Contents lists available at ScienceDirect

Extreme Mechanics Letters

Experimental and computational analysis of the injection-induced mechanical changes in the skin microenvironment during subcutaneous injection of biologics

Yingnan Shen [a],[1], Sameep Rajubhai Shah [a],[1], Kejie Zhao [a], Bumsoo Han [a],[b],[c],*

[a] *School of Mechanical Engineering, Purdue University, West Lafayette, IN, USA*
[b] *Weldon School of Biomedical Engineering, Purdue University, West Lafayette, IN, USA*
[c] *Purdue Institute for Cancer Research, Purdue University, West Lafayette, IN, USA*

A R T I C L E   I N F O

A B S T R A C T

Subcutaneous (SQ) injection is an effective delivery route for various biologics, including proteins, antibodies, and vaccines. However, pain and discomfort induced during SQ injection pose a notable challenge for the broader and routine use of biologics. Understanding the underlying mechanism and quantification of injection-induced pain and discomfort (IPD) are urgently needed. A crucial knowledge gap is what changes in the skin tissue microenvironment are induced by the SQ injection, which may ultimately cause the IPD. In this study, thus, a hypothesis is postulated that the injection of biologics solution through the skin tissue microenvironment induces spatiotemporal mechanical changes. Specifically, the injection leads to tissue swelling and subsequent increases in the interstitial fluid pressure (IFP) and matrix stress around the injection site, which ultimately causes the IPD. To test this hypothesis, an engineered SQ injection model is developed capable of measuring tissue swelling during SQ injection. The injection model consists of a skin equivalent with quantum dot-labeled fibroblasts, which enables the measurement of injection-induced spatiotemporal deformation. The IFP and matrix stress are further estimated by computational analysis approximating the skin equivalent as a nonlinear poroelastic material. The result confirms significant injection-induced tissue swelling and increases in IFP and matrix stress. The extent of deformation is correlated to the injection rate. The results also suggest that the size of biologics particulates significantly affects the pattern and extent of the deformation. The results are further discussed to propose a quantitative understanding of the injection-induced changes in the skin microenvironment.

© 2023 Elsevier Ltd. All rights reserved.

1. Introduction

Biologics, pharmaceutical products derived from biological origin, are rapidly emerging because of superior efficacy and low toxicity. These drugs include recombinant proteins, antibodies, vaccines, blood components, and reprogrammed cells [1–4]. Recently, eight of the top ten selling drugs globally are biologics [5]. However, the effective delivery of biologics is still challenging due to the large molecular weights and the sensitive molecular structure to the environmental condition. Intravenous delivery may be effective, but it typically needs to be administered by medical professionals which substantially increases the treatment cost and burden [6]. In this context, subcutaneous (SQ) injection has been considered a promising delivery route because it can be self-administered [7]. SQ administration has been approved for more than 100 biologics, and many more clinical trials are currently ongoing [8]. Biologics often require repeated SQ injection for a prolonged period. One of the most critical drawbacks, however, pain and discomfort are induced during SQ injection. This injection-induced pain and discomfort (IPD) poses significant hurdles for the broader use of biologics, the design of injection devices and drug formulations, and the quality of patients' life [9–11].

However, the underlying mechanism of the IPD is not well understood yet. Patients reported severe IPD during SQ injection, not the sting of the needle [12,13]. To assess the impact of SQ injection, current studies rely on pain intensity scales which include the faces pain scale (FPS), the numerical rating scale (NRS), the verbal rating scale (VRS) and the visual analogue scale (VAS) [14,15]. The commonly used pain intensity scale of FPS, NRS, VRS or VAS are based on patient self-rating, the subjectivity of which may lead to controversial conclusions. For instance, when injecting Tralokinumab, a monoclonal antibody treating

---

asthma, the slower injection rate was associated with lower self-reported measure of pain intensity [16], while injection rate had no significant impact on the self-reported measure of pain intensity during a SQ injection test on patients with diabetes [10]. Thus, the mechanistic understanding and quantification of the IPD is highly desirable for the design of formulation and SQ injection protocols of biologics to minimize the IPD. Although the IPD is thought to be a nociceptive pain which can be generated by the nociceptors in the dermis upon the mechanical microenvironment changes [17], no clear correlation of the extent of IPD to the mechanical changes in the skin tissue microenvironment.

This study aims to quantify the mechanical changes of the skin tissue microenvironment during SQ injection to establish a quantitative understanding of the injection-induced mechanical cues in the skin tissue. This is based on a hypothesis that the injected biologics solution, i.e., biologics particulates in suspension, induces changes in the mechanical microenvironment of the skin tissue. Specifically, the injection leads to local tissue swelling and subsequent increases in the interstitial fluid pressure (IFP) and matrix stress around the injection site, which ultimately causes the IPD. To test this hypothesis, an engineered SQ injection model is developed capable of measuring tissue swelling during SQ injection. This model consists of a skin equivalent constructed by seeding quantum dot (QD)-labeled fibroblasts in a collagen extracellular matrix (ECM). The skin equivalents were subjected to injection mimicking the SQ injection scenario, while the model was under time-lapsed imaging. The images were analyzed to estimate the tissue deformation. The changes in IFP and matrix stress were studied by computational analysis which approximates the model to a nonlinear poroelastic material. Effects of injection rates and size of biologics molecules on the magnitudes and distributions of these mechanical microenvironment changes are further studied. Based on the results, the mechanistic parameters of displacement rate, total displacement, IFP, and matrix stress are discussed as potential biomarkers.

2. Materials and methods

2.1. Experimental setup for injection-induced tissue deformation measurements

An experimental method named cell image deformetry (CID) was used to measure the spatiotemporal deformation of engineered tissue construct (ETC) during the injection of model biologics. The CID method was also described in our previous work on tissue deformation during freezing [18]. A schematic of the experimental platform constructed for CID is shown in Fig. 1A. The platform consists of an injection system, an imaging system, and ETC. The imaging system includes a fluorescence macro/microscope (MVX10, Olympus, PA) equipped with a TRITC filter, a CCD camera (Aqua, QImaging, CA), and a fluorescent illuminator (X-Cite 120Q, Excelitas Technologies, MA). The injection system includes a syringe pump (NE 1000, New Era Pump Systems, NY) which controls the injection flow rates, as well as a three-axis micromanipulator which adjusts the needle orientation and insertion depth into the ETC.

2.2. Design and fabrication of the engineered SQ injection model

An engineered SQ injection model to mimic the deformation of skin's dermal layer during SQ injection was developed based on our previous studies [18–21]. As shown in Fig. 1B, the model includes an ETC, as well as proper physical constraints on the ETC mimicking the SQ injection scenario. Overall, the ETC simulates the injection area in skin including dermis and subcutaneous

tissue, the Polydimethylsiloxane (PDMS) layer simulates the epidermis as a tough and protective sheath, and the agar ring and agar layer simulate the tissue surrounding the injection area. Specifically, PDMS fulfills the mimicry of the elastic modulus of epidermis. Both PDMS and epidermis have the elastic modulus of 1 to 2 MPa [22,23]. Type I collagen gel at the concentration of 6 mg mL^{-1} is used to simulate the SQ tissue of the injection area, whose tensile elastic modulus is comparable to subcutaneous tissue which is around 50 kPa [24–26]. 1.15% agar gel, whose compressive elastic modulus is around 50 kPa [27], is used to simulate the SQ tissue surrounding the injection area. The fabrication process of the engineered tissue model is as follows:

A PDMS ring attached on a thin (1 mm) PDMS layer was firstly built as the skeleton of the model, then an agar ring was created inside the PDMS ring, which was also attached on the thin PDMS layer. Then, 1 mL collagen solution suspended with the QDs-labeled fibroblasts was placed in the cylindrical hole (10 mm in diameter) surrounded by the agar ring, followed by polymerization at 37 °C for 90 min. The collagen solution was prepared from a high concentration type I rat tail collagen (Corning, Bedford, MA), which contained 6 mg mL^{-1} collagen, 10% v/v 10X PBS, 2.3% (v/v of collagen added) 1 N sodium hydroxide, 30 mM HEPES, 6% v/v fetal bovine serum, 10 μg mL^{-1} penicillin/streptomycin, 2 mM L-glutamine, and distilled water (added to make a total volume of 1 mL). The preparation of a neutralized collagen solution was also described in our previous work [18–21]. The 1 mL collagen solution was mixed with QDs-labeled fibroblasts at the cell seeding density of 2×10^5 cells mL^{-1}. After polymerization, the engineered tissue construct was incubated in complete culture medium at 37 °C and 5% CO$_2$ for 2 days. After incubation, the cylindrical ETC still adhered to the agar ring, with a diameter of 10 mm and a thickness of 10.2 ± 0.2 mm ($n = 3$).

2.3. Human dermal fibroblasts culture in ETC

Human dermal fibroblasts were maintained in DMEM/F12 medium (Invitrogen, NY) supplemented by 10% v/v fetal bovine serum, 2 mM L-glutamine, and 100 μg mL^{-1} penicillin/streptomycin. The fibroblasts were cultured in 75 cm^2 T-flasks at 37 °C and 5% CO$_2$, and routinely harvested at 80-90% confluency by using 0.05% trypsin and 0.53 mM EDTA, used for experiments or subculture. The cells were maintained up to 19th passage during the experiments, and 2×10^5 cells were collected for the cell seeding in each ETC. The collected fibroblasts were labeled with quantum dots (Qtracker 655, Invitrogen, Carlsbad, CA) according to a protocol suggested by the manufacturer. Fig. 1B shows a fabricated injection model and QD-labeled cells embedded in ETC. After 2 day incubation, the fibroblasts cultured in collagen developed dendritic morphology, and the overlay of brightfield and TRITC images confirmed that quantum dots specifically accumulated in the cytoplasm of fibroblasts.

2.4. Tissue deformation measurement during injection

Distilled water was injected through a 27-gauge hypodermic needle into the ETCs at different flow rates of 0.6, 1.2, and 2.5 mL min^{-1}. The model biologics were injected at a flow rate of 1.2 mL min^{-1}. For each injection experiment, the ETC surface was kept at 45 degrees, and the needle was inserted into the ETC at a fixed depth of 4 mm. Before the injection experiments, the culture medium was removed, and an agar layer was created on the agar ring as well as the ETC. Both the agar ring and agar layer were formed from the gelation of 1.15% agarose solution, and the solution temperature should decrease till 37 °C before loaded on the ETC. Finally, the engineered tissue model was
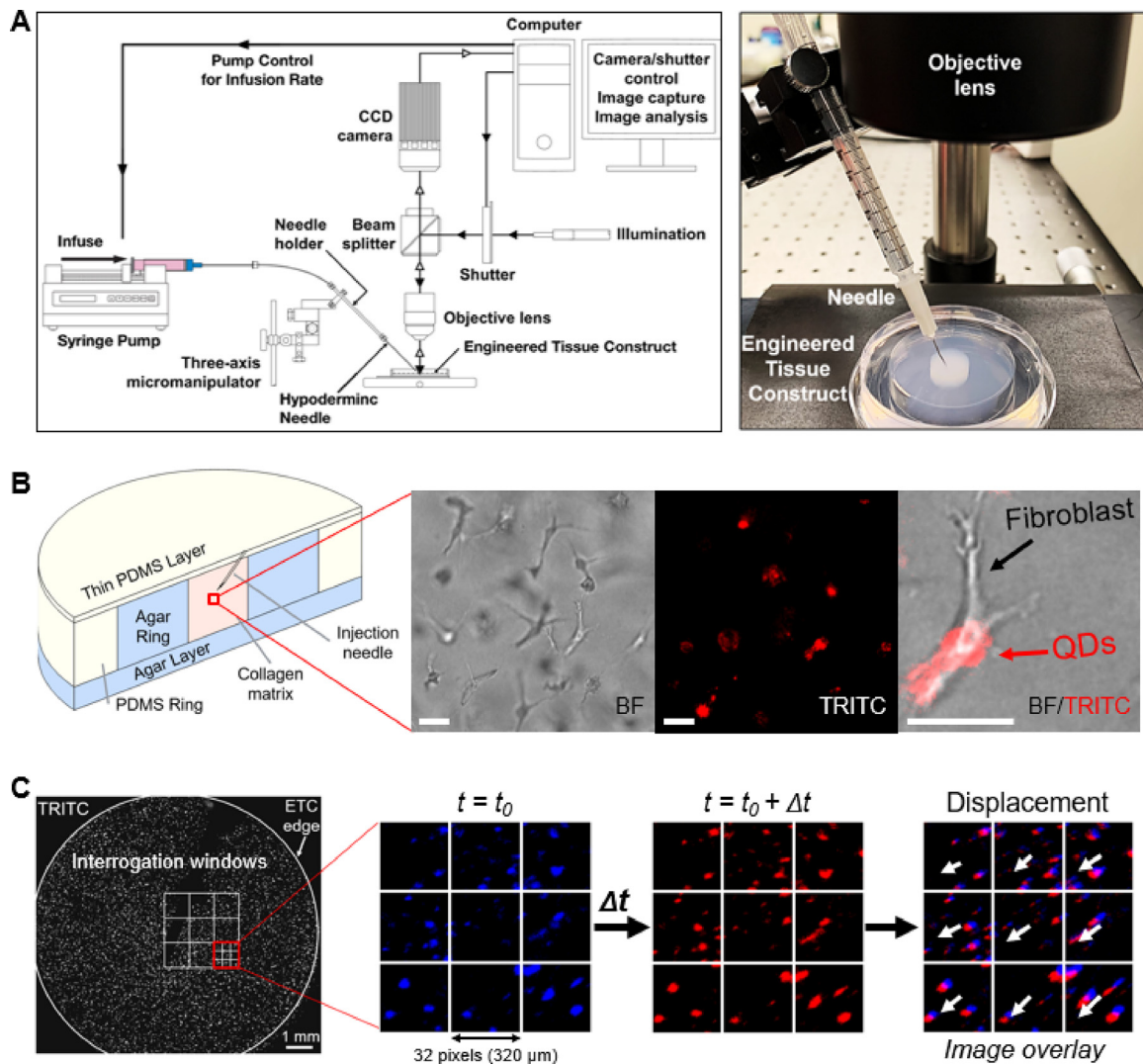
Fig. 1. Engineered SQ injection model to mimic injection-induced tissue swelling. (A) Schematic and image of the experimental setup constructed for CID, including an injection system, an imaging system and ETC. (B) Schematic of the conceptual design: The ETC simulates the injection area in skin including dermis and subcutaneous tissue. The PDMS layer simulates the epidermis as a tough and protective sheath. The agar ring and agar layer simulate the tissue surrounding the injection area. Scale bar: 50 μm. QD-labeled fibroblasts are embedded in the collagen matrix. Overlay of brightfield and TRITC images confirms that quantum dots specifically accumulate in the cytoplasm of dendritic fibroblasts. (C) Measurement of the deformation of ETC using the CID method. The acquired fluorescence image was divided into 32 × 32 pixels interrogation windows. Overlaying and cross-correlating the fluorescence images taken Δt apart provides the displacement rate vector. The number of fluorescence particles in a single interrogation window was no less than 3 to guarantee the quality of cross-correlation.

placed on a dish for the injection experiments. Additional details of the step-by-step fabrication processes are provided in **Fig. S1** in supplementary material. Time-lapse fluorescence images of the top view of ETC were acquired every 0.05 s during the injection. The focal plane was adjusted to the needle tip in the ETC. The acquired sequential images were divided into 32 × 32 pixels interrogation windows and cross-correlated at a time interval Δt to estimate the displacement rate $\Delta u/\Delta t$ using DaVis software (LaVision, Ypsilanti, MI). As shown in Fig. 1C, the number of fluorescence particles in a single interrogation window was at least 3 to guarantee the quality of cross-correlation. The ETC is assumed to be undeformed right before the injection ($t = 0$), and each interrogation window represents a material point at $t = 0$. The grid of the material points enabled the calculation of the displacement rate field at a resolution of 320 μm for the first time interval of $t = 0 \sim \Delta t$. The displacement rate fields of the material points at later time points were approximated by interpolation of the cross-correlation results of Δu, based on which the total displacement field can be estimated by integrating the displacement rate fields of the material points.

2.5. Model biologics preparation

Model biologics were prepared by dissolving fluorescein isot-hiocyanate–dextran (FD4/FD500S, Millipore Sigma, Burlington, MA) in distilled water. Smaller dextran (FD4) with an average molecular weight (MW) of 4 kDa was solubilized at the concentration of 5 mg/mL, which is similar to small-MW biologics such as insulin [28]. Larger dextran (FD500S) with an average MW of 500 kDa was solubilized at the concentration of 50 mg/mL, which is similar to large-MW biologics such as drug-conjugated mon-oclonal antibodies, botulinum toxin with complexing proteins, and polymeric IgA antibodies [29–31]. The model biologics were injected through a 27-gauge hypodermic needle into the ETCs at a flow rate of 1.2 mL min^{-1}.

2.6. Computational analysis of the injection-induced ETC deformation, IFP and stress

We present a multi-physics coupled computational framework to simulate the variation in the ETC microenvironment brought by

the SQ injection, and to further predict the surface and internal three-dimensional distribution of IFP and matrix stress fields. The tissue is considered as poroelastic biphasic material, with non-linear elastic deformable porous solid and fluid saturated pores. The framework integrates interstitial fluid flow, tissue deformation, and mechanics based on finite deformation hyperelasticity to model the nonlinear response. In this section we describe the governing equations, inter-physical coupling, and boundary conditions. The computational domain (Fig. 1B) mimics the experimental setup described before, in 3D. The mechanical governing equations are numerically solved in all the sub-domains while the fluid flow equations are solved only in the ETC and agar sub-domains. The computational domain is discretized using an unstructured 3D tetrahedral mesh (Fig. 4A) with extremely fine elements close to the needle and injection location in the collagen. A transient study simultaneously, numerically solves the governing equations using the MUltifrontal Massively Parallel sparse direct (MUMPS) solver in COMSOL Multiphysics 5.4.

2.6.1. Conservation of mass and interstitial fluid flow

The conservation of mass for the biphasic tissue is given as

$$\frac{\partial (\phi_\alpha \rho_\alpha)}{\partial t} + \nabla \cdot (\phi_\alpha \rho_\alpha \boldsymbol{v}_\alpha) = \widehat{q_\alpha} \tag{1}$$

where the index α represents different phases: solid, s and fluid, f, ρ is the density, and $\boldsymbol{v}$ is the velocity. Based on the assumption that the pores are saturated with the fluid, the volume fractions, ϕ, must follow the condition $\phi_f + \phi_s = 1$. Assuming incompressibility of the phases, and that solid phase source $\widehat{q_s} = 0$, the combined conservation of mass for the tissue [32,33] reduces to

$$\nabla \cdot \boldsymbol{v}_s + \nabla \cdot (\phi_f (\boldsymbol{v}_f - \boldsymbol{v}_s)) = q_f \tag{2}$$

where $q_f = \widehat{q_f}/\rho_f$. Here the velocity of the solid phase, $\boldsymbol{v}_s$ is the time derivative of the deformation vector $\boldsymbol{u}$. Assuming the fluid flow follows Darcy's law, the Darcy velocity $\boldsymbol{w}$ is related to the pressure gradient:

$$\boldsymbol{w} = \phi_f (\boldsymbol{v}_f - \boldsymbol{v}_s) = -\frac{\kappa}{\mu_f} \nabla p \tag{3}$$

where μ_f is the dynamic viscosity, and p is the fluid pressure. The Darcy permeability κ is assumed to be constant. The fluid volume fraction ϕ_f, also known as the porosity, is evolving and deformation dependent [32,33]:

$$\phi_f = 1 - \phi_s = 1 - \frac{\phi_{s,0}}{J_s} \tag{4}$$

where $\phi_{s,0}$ is the initial solid volume fraction, and $J_s = \det(\boldsymbol{F}_s)$ is the Jacobian determinant of the solid deformation gradient tensor $\boldsymbol{F}_s$.

At the syringe needle tip, an inward mass flux is defined as

$$-\boldsymbol{n} \cdot \rho \boldsymbol{v}_f = N_0 \tag{5}$$

where $\boldsymbol{n}$ is the outward normal, and N_0 is the constant value calculated based on the injection rate. At all other external surfaces of the collagen and agar sub-domains, a no flow boundary condition is implemented as $-\boldsymbol{n} \cdot \rho \boldsymbol{v}_f = 0$.

2.6.2. Conservation of linear momentum and tissue deformation

Assuming the absence of acceleration terms and body forces, the conservation of linear momentum for the tissue is defined as

$$\nabla \cdot \boldsymbol{\sigma} = 0 \tag{6}$$

where $\boldsymbol{\sigma}$ is the combined Cauchy stress tensor which is influenced by the pore pressure p,

$$\boldsymbol{\sigma} = \boldsymbol{\sigma}_E - p\boldsymbol{I} \tag{7}$$

Here, $\boldsymbol{\sigma}_E$ is the elastic stress tensor.

ETC is considered as a nonlinear hyperelastic material and the three term Ogden model is adopted where the strain energy function Ψ is defined as

$$\Psi = \sum_{i=1}^{3} \frac{\mu_i}{\alpha_i} \left[\lambda_1^{\alpha_i} + \lambda_2^{\alpha_i} + \lambda_3^{\alpha_i} - 3 \right] \tag{8}$$

Here, α_i and μ_i are material parameters and $\lambda_1, \lambda_2, \lambda_3$ are isochoric principal stretches. The elastic Cauchy stress tensor for ETC can be obtained from the Kirchhoff extra stress tensor $\boldsymbol{\tau}_E$ as

$$\boldsymbol{\sigma}_E = \frac{\boldsymbol{\tau}_E}{J_s} = \frac{1}{J_s} \boldsymbol{F}_s \left(2 \frac{\partial \Psi}{\partial \boldsymbol{C}_s} \right) \boldsymbol{F}_s^T \tag{9}$$

where $\boldsymbol{C}_s$ is the right Cauchy–Green deformation tensor defined as $\boldsymbol{C}_s = \boldsymbol{F}_s^T \boldsymbol{F}_s$. Agar and PDMS are assumed to be linear elastic such that they follow the relation

$$\boldsymbol{\sigma}_E = \mathbb{C} : \boldsymbol{E}_s \tag{10}$$

where $\mathbb{C}$ is the isotropic stiffness tensor that is defined using the elastic modulus E and Poisson's ratio ν, and $\boldsymbol{E}_s = (\boldsymbol{C}_s - \boldsymbol{I})/2$ is the Green–Lagrange strain tensor. Lastly, the surfaces in contact with the needle are assumed to be fixed, $\boldsymbol{u} = 0$. The lower surface of the agar base is restricted from deforming in the z direction (normal to the surface). All other surfaces are free to deform. Making use of the symmetry in the model system, only half the domain needs to be used and symmetry boundary conditions are included in all the separate physics involved. The material properties used for computational analysis are provided in Table 1.

2.7. Statistical analysis

The spatiotemporal analysis of the injection-induced changes in tissue's mechanical microenvironment was performed using the software OriginPro V2019b (OriginLab, Northampton, MA, USA). The quantification of displacement rate and total displacement was performed on the data acquired from the injection tests carried out in triplicate. The statistical analysis of displacement rate and total displacement was performed using the software GraphPad Prism 8 (GraphPad Software, San Diego, CA, USA). The data are presented as means $\pm$ the standard deviation. The quantification of IFP and matrix stress was performed on the data acquired from the computational analysis of SQ injection. The computational tissue deformation, pressure and stress data at the horizontal and vertical cross sections of the simulated ETC were extracted for the quantification.

3. Results

SQ injection induces significant spatiotemporal tissue deformation. Fig. 2A shows the raw time-lapse fluorescence images of the top view of ETC when distilled water is injected at a rate of 1.2 mL min^{-1} into ETC. The outline of the needle is indicated with a dashed line in the first image while the injection site is noted with the dot, and the injection direction is indicated with the arrow. These acquired images are divided into smaller interrogation windows and cross-correlated with the state of ETC right before injection ($t = 0$ s), assumed to be the reference state. Fig. 2B shows the displacement rate vector field measured by the CID method. Significant tissue deformation occurred in the first 0.2 s since the start of injection, during which local displacement rate reached above 800 μm s^{-1} in the region around the injection site. Although the magnitude of displacement rate substantially reduced at 0.3 and 0.4 s, the size of deformed tissue continues to enlarge such that the maxima of displacement rate and deformation occur at different time points. The total displacement field

Table 1

Material properties used for computational analysis.

Material	Mechanical properties	Darcy permeability (m^2)	Porosity
6 mg/mL collagen gel	$\mu_1 = 0.345$ MPa $\alpha_1 = 0.857$ $\mu_2 = 1.03$ kPa $\alpha_2 = 3.264$ $\mu_3 = -0.338$ MPa $\alpha_3 = 0.703$ [34]	10^{-13} [35–37]	0.94 [38]
1.15% (w/v) agarose gel	$E = 48$ kPa [27] $\nu = 0.499$ [27]	10^{-15} [39]	0.98 [40]
PDMS	$E = 2000$ kPa [23] $\nu = 0.499$ [23]	–	–
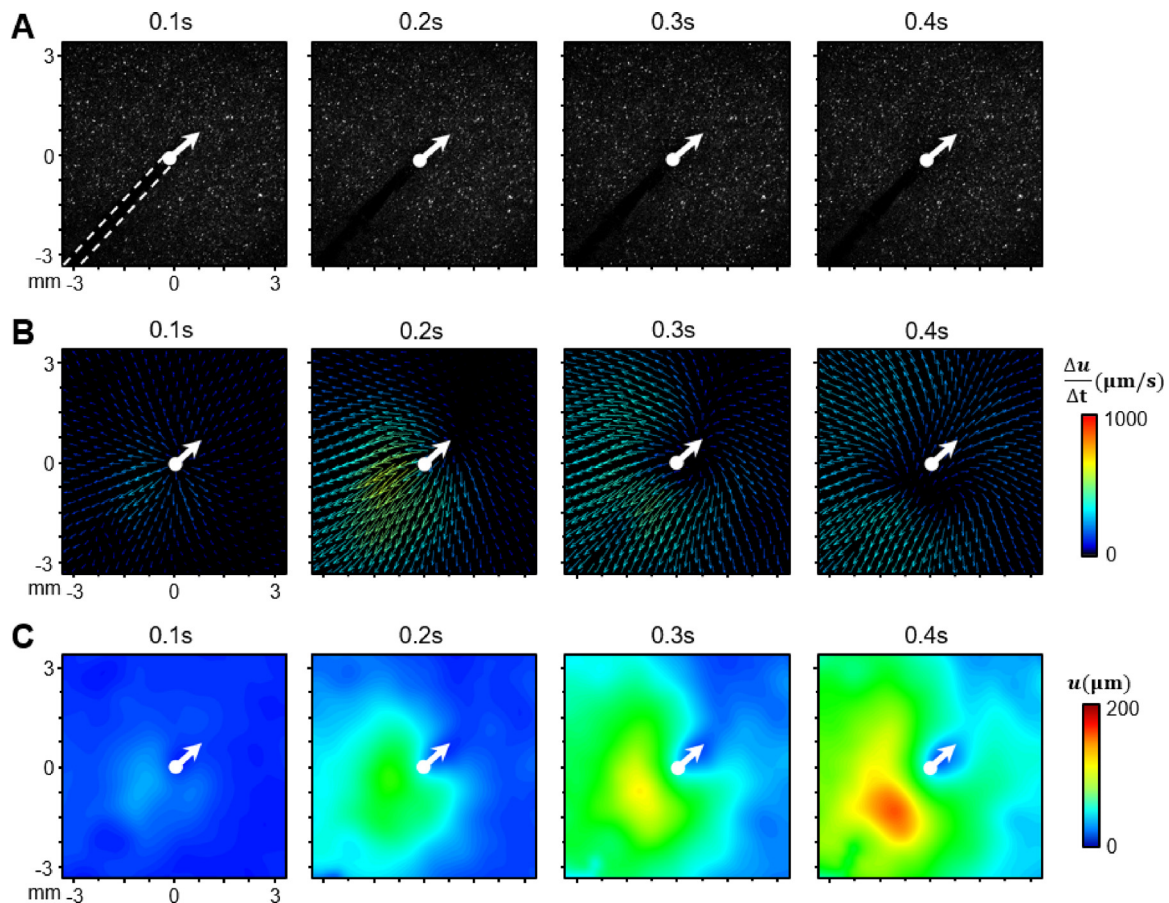
Fig. 2. Significant injection-induced tissue deformation shown by CID measurements. (A) Fluorescent micrographs with QD distribution (B) Local displacement rate ($\Delta u/\Delta t$) vector field and (C) total displacement (u) field during the injection of water into ETC at 1.2 mL min^{-1} from $t = 0.1$ s to $t = 0.4$ s. $t = 0$ s represents the start of injection. The white dashed line (A) indicates the needle. The injection site and injection direction are indicated by the white dot and the white arrow, respectively.

provided in Fig. 2C shows the localized deformation around the injection site with a displacement larger than 160 μm. This result demonstrates the injection induces significant tissue deformation around the injection site.

The injection flow rate has been thought as one of the important factors to optimize the injection protocol to maintain the injection-induced pain at a tolerable range [16]. The extent and magnitude of the injection-induced changes in the mechanical microenvironment are anticipated to vary significantly depending on the flow rates. The experimentally observed effects of injection flow rates on the tissue deformation are presented in Fig. 3. In comparison to the 1.2 mL min^{-1} injection, experimental measurements on the ETCs at the injection rates of 0.6 mL min^{-1} (Fig. 3A) and 2.5 mL min^{-1} (Fig. 3B) were performed to delineate the effect of injection rate on tissue deformation which

is characterized by local displacement rate ($\Delta u/\Delta t$) and total displacement (u).

The displacement rate vector fields in Fig. 3 shows significant increase of displacement rate with increasing injection flow rate. The maximum local displacement rate occurred around the injection site at $t = 0.2$ s since the start of injection, and quantitatively, it increased from 388 ± 65 to 1104 ± 74 μm s^{-1} with increasing injection rate from 0.6 to 2.5 mL min^{-1}. The total displacement fields provided in Fig. 3 show significant increase of tissue deformation with the increase of injection rate. At 0.4 s, the maximum total displacement around the injection site increased from 67 ± 27 to 231 ± 51 μm with increasing injection rate from 0.6 to 2.5 mL min^{-1}. As shown in Fig. 2, the moderate injection rate of 1.2 mL min^{-1} generated moderate-magnitude displacement rate and total displacement, the local
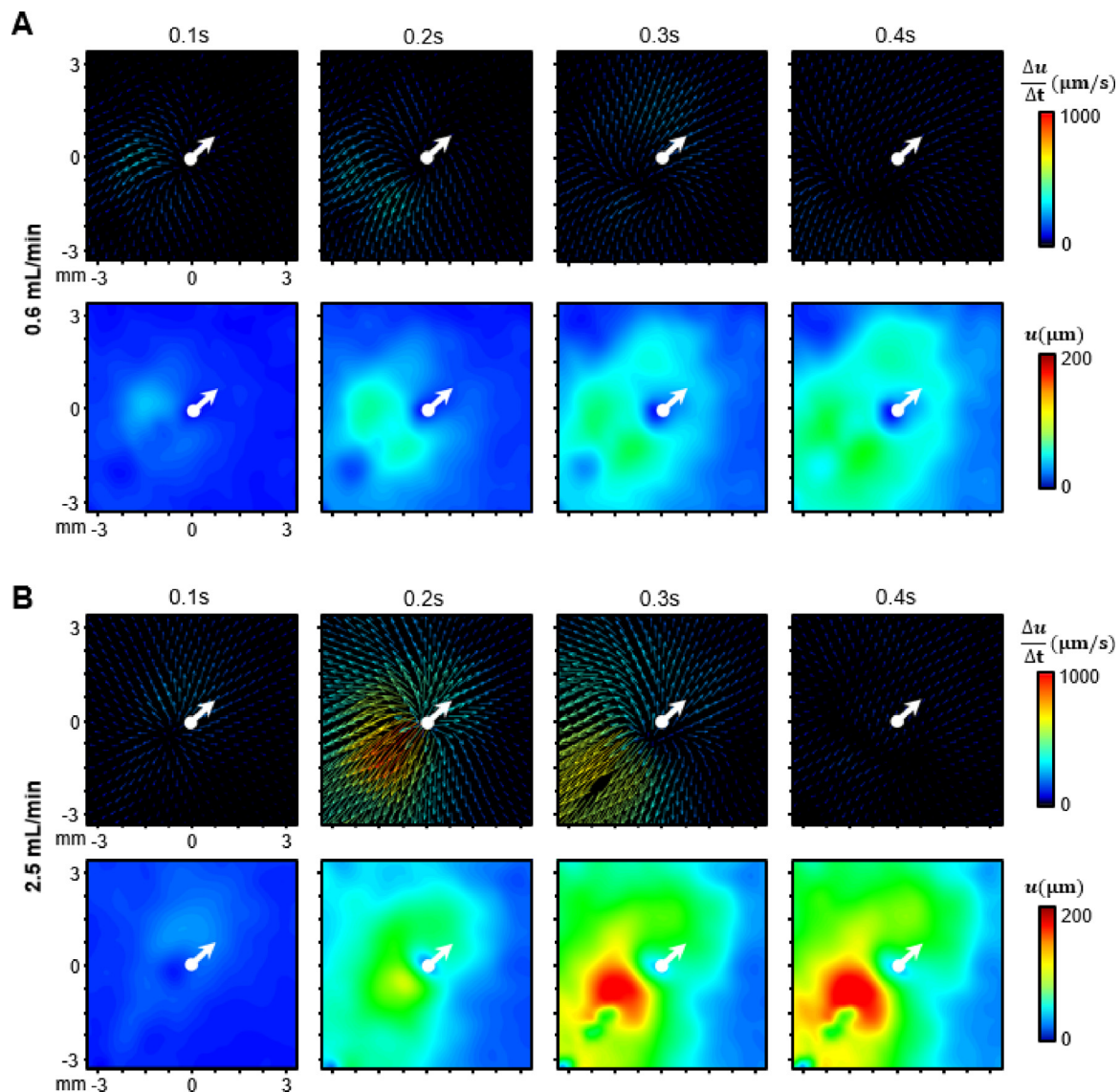
Fig. 3. Experimental measurements of tissue deformation of the ETCs at different injection rates. Local displacement rate ($\Delta u / \Delta t$) vector field and total displacement (u) field during the injection at (A) 0.6 mL min^{-1} and (B) 2.5 mL min^{-1} from $t = 0.1$ s to $t = 0.4$ s. $t = 0$ s represents the start of injection. The injection site and injection direction are indicated by the white dot and the white arrow, respectively.

maxima of which were 645 ± 194 μm s^{-1} and 157 ± 28 μm, respectively. The total displacements were also radially averaged for the comparisons of the spatiotemporal changes at different injection rates (**Fig. S2**). The radially averaged total displacement $\overline{u_r}$ is the average value of the total displacements at the locations having the same distance of r to the injection site. The maximum $\overline{u_r}$ at 0.4 s were approximately 60, 90, and 120 μm at the injection rates of 0.6, 1.2, and 2.5 mL min^{-1}, respectively.

Computational results of deformation of ETC induced by the injection of water at 1.2 mL min^{-1}, is shown in Fig. 4. The computational results allow the visualization of the injection-induced mechanical changes throughout the ETC, which cannot be obtained by the experimental measurements using CID method. Fig. 4B shows 3D distribution of the deformation field at $t = 0.4$ s, over a 3D cutout of the ETC domain. The maximum deformation occurs just behind the injection site with the remaining ETC also undergoing significant deformation. The tissue swelling also leads to a bulge on the top surface of ETC. The plane of cross-section used to visualize the top view in computational analysis is matched with the experimental focus plane at the needle tip. The planes of cross-section for both the top and side

view are indicated with dotted planes in Fig. 4B. Top view of the computational result shown in Fig. 4C can be compared with the experimental measurements. Similar to experimental observation, the maximum deformation occurs along the injection direction, but behind the injection site. Additionally, significant tissue deformation occurred in the first 0.2 s around the injection site of the computational model, and the size of deformed tissue continues to enlarge at 0.3 and 0.4 s. Fig. 4C shows the side view of the tissue deformation, with significant deformation beneath the needle tip, with a growing comma shaped deformation of the tissue surrounding the site of injection. The quantitative comparison between experimental measurements and computational analysis is shown in **Fig. S3**. The total displacement data along the injection direction (noted as "A") and the perpendicular direction (noted as "P") at $t = 0.4$ s were extracted and plotted. Both the experimental and computational results show larger tissue deformation along the injection direction than the perpendicular direction. Moreover, along the injection direction, both the experimental and computational results show larger tissue deformation behind the injection site than in front of the injection site.
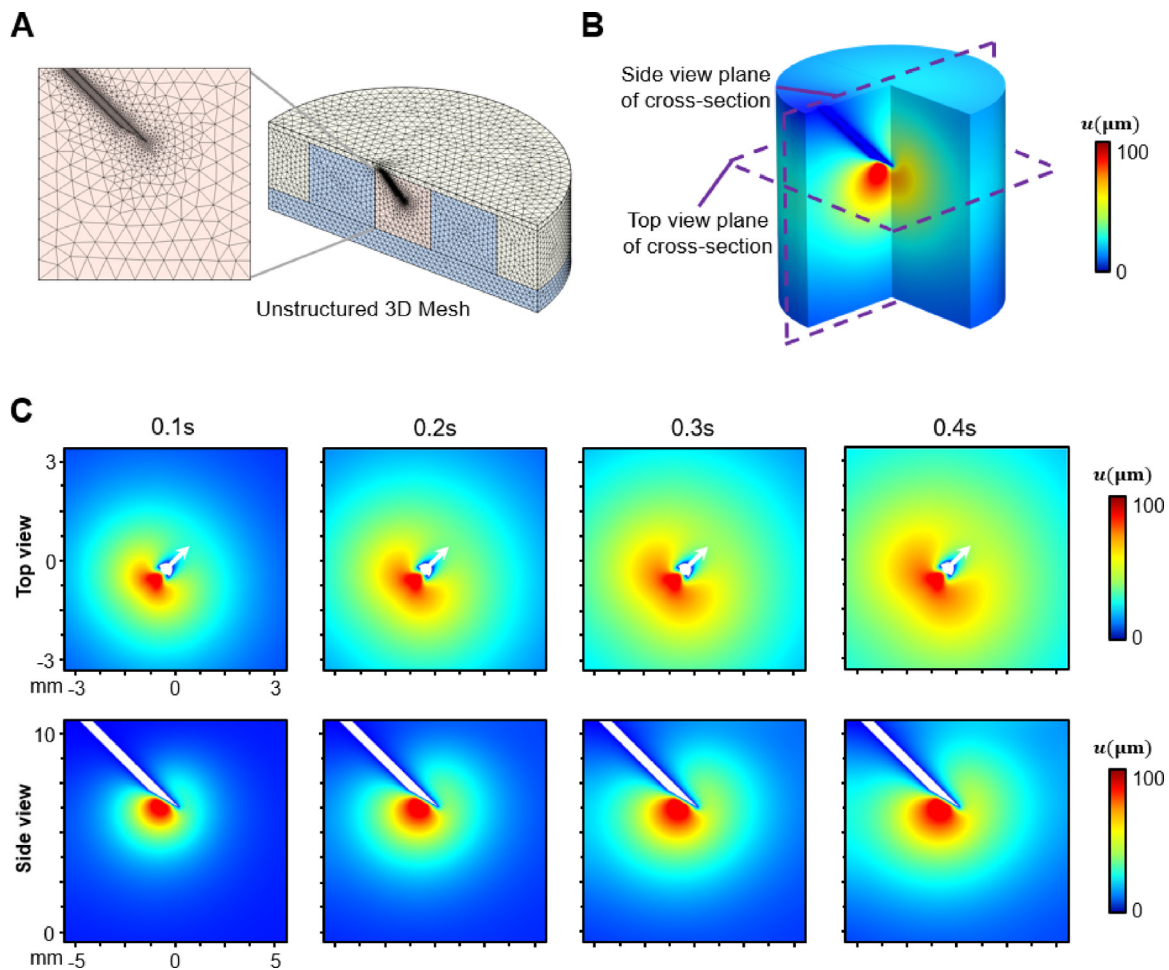
Fig. 4. (A) The 3D unstructured mesh used for the computational analysis. (B, C) Significant injection-induced tissue deformation shown by computational analysis. (B) 3D distribution of displacement (u) field in ETC for 1.2 mL min^{-1} at $t = 0.4$ s. (C) Computational top view and side view of total displacement field of ETC during the injection of water at 1.2 mL min^{-1} ($t = 0.1$ s to 0.4 s).

Fig. 5 shows computational results at different injection rates of 0.6 mL min^{-1} and 2.5 mL min^{-1} which follow the same trend as the experimental results as seen in Fig. 3. The magnitude of deformation is directly dependent on the flow rate. The tissue deformation extent around the injection site, as well as deformed tissue area increases as the injection rate increases. The majority of the deformation occurs initially at the start of the injection, in the immediate vicinity of the needle tip. Maximum deformation occurs behind the injection site, with the rest of the tissue experiencing relatively lower deformation. The tissue deformation then slowly increases as the injection proceeds. While parts of the tissue remain close to undeformed at 0.6 mL min^{-1}, the spread of the deformation field in all directions is much larger at a higher flow rate of 2.5 mL min^{-1} as seen in both the top and side views . This behavior is more evident in the side view where the maximum deformation occurs under the needle tip within 0.1 s, but by the end of the injection at 0.4 s, significant deformation has occurred at the top surface of the ETC as well. **Fig. S3** provides the quantitative comparison between experimental measurements and computational analysis of the injection-induced deformation of ETC at the injection rates of 0.6 and 2.5 mL min^{-1}. Similar to the 1.2 mL min^{-1} injection result, the 0.6 and 2.5 mL min^{-1} injections induced larger tissue deformation along the injection direction than the perpendicular direction, as well as larger tissue deformation behind the injection site than in front of the injection site.

Fig. 6 shows the effect of the injection rate on the IFP (p) and von-Mises equivalent stress (σ_e) studied by computational

analysis. The 3D distribution of the IFP and stress for the injection rate of 1.2 mL min^{-1} at $t = 0.4$ s is presented in Fig. 6A. Compared to the distribution pattern of the deformation, both IFP and equivalent matrix stress fields are more localized close to the injection site. Fig. 6B shows the effect of varying flow rate on IFP and matrix stress fields at the injection rates of 0.6, 1.2, and 2.5 mL min^{-1}. The maximum p and σ_e reach 68 and 90 kPa, respectively, at 2.5 mL min^{-1}. However, at lower injection rates, the maxima are significantly smaller. The stress distribution in the tissue is under mostly <10 kPa, with the maxima of 90 kPa occurring at the needle tip due to stress concentration and fixed boundary condition of the needle in computation. The peak values of pressure occur at the injection site as well. The region in the immediate vicinity of the injection site, in the direction of injection, experiences high p and σ_e. The size of this region and the peak values of p and σ_e are directly dependent on the injection rate. However, both p and σ_e drastically drop to very small values, away from this region. The corresponding animations of the computational result are provided in the supplementary material.

Fig. 7 shows that the injection of different-MW model biologics, 4 and 500 kDa dextran solutions, induces distinct distributions of dextran, as well as tissue deformations. The spatial distribution patterns of model biologics in ETCs are shown in Fig. 7A. Interestingly, the patterns are distinctly different depending on the molecular weight of model biologics. 4 kDa dextran transports preferentially along the injection direction. In contrast, 500 kDa dextran is transported more perpendicular to the injection direction. Moreover, 500 kDa dextran appears to be accumulated at the
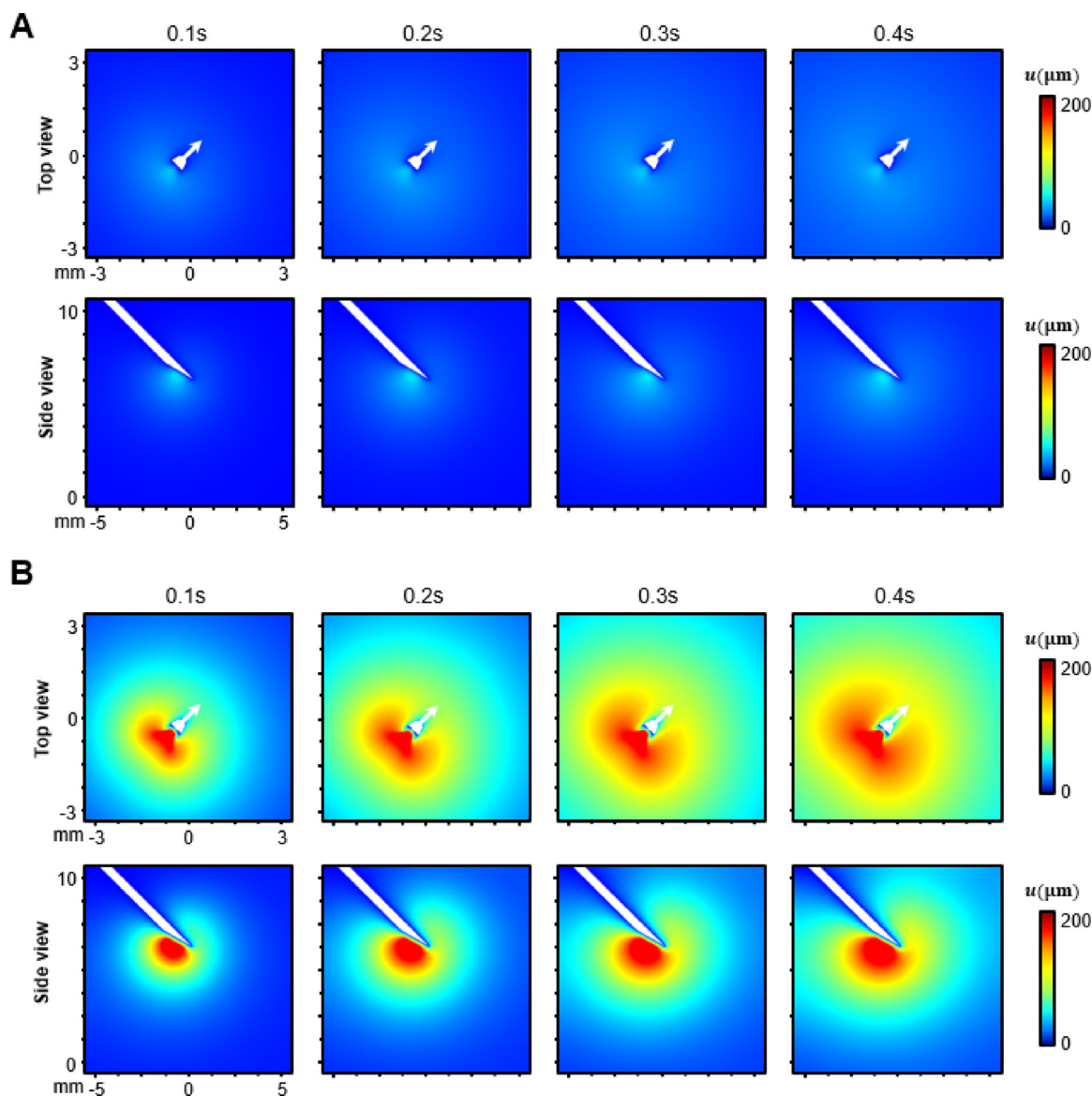
Fig. 5. Computational results of the total displacement field of the ETCs at different injection rates of (A) 0.6 mL min^{-1} and (B) 2.5 mL min^{-1}.

transport front, noted with a triangle. These patterns suggest that the smaller model biologics convects through the pores of the ETC, but the larger model biologics may clog the pores along the injection direction and is diverted to the perpendicular direction.

Displacement rate and displacement fields, induced by the injections of model biologics of 4 and 500 kDa dextran solutions, are shown in Fig. 7B and Fig. 7C, respectively, at the injection rate of 1.2 mL min^{-1}. The displacement of 4 kDa injection case rapidly increased in the first 0.4 s, and tissue deformation mainly distributed along the injection direction. The increase of displacement of 500 kDa injection case was slower but continued up to 0.8 s possibly due to lower fluid mobility. Compared to 4 kDa injection, the shape of the deformed region at 500 kDa injection was distinctly different and had a kidney shape. The spatial pattern of 500 kDa dextran transport shown in Fig. 7A may provide an explanation of the kidney shape of tissue deformation.

4. Discussion

The knowledge gap between the SQ administration and the injection-induced pain makes it impossible to identify predictive biomakers to guide the formulation design and SQ injection

protocol of various biologics for pain minimization. The injection-induced pain is considered as mechanical pain, however, little is known about the mechanical microenvironment changes during the SQ injection. To take a critical step to bridge this knowledge gap, this study develops a SQ injection model based on an in vitro method utilizing the CID technique and the poroelastic theory on engineered dermal equivalents, which enables the quantitative analysis of the mechanical microenvironment changes and their correlation with the SQ injection conditions.

The present study demonstrates that SQ injection causes distinct spatiotemporal changes in the mechanical microenvironment. Based on the measurement of tissue deformation and the calculation of fluid transport in the poroelastic ETC, the mechanical microenvironment changes are identified into four types of potential biomarkers, including the experimentally measured displacement rate and total displacement, as well as the computationally analyzed IFP and matrix stress. These mechanical microenvironment changes are thought to activate nociceptors and induce pain, which can be compared with different types of mechanical stimuli studied on the responses of nociceptors.

The rate of displacement is a biologically relevant parameter of mechanical stimulation [17]. The peak value of the voltage
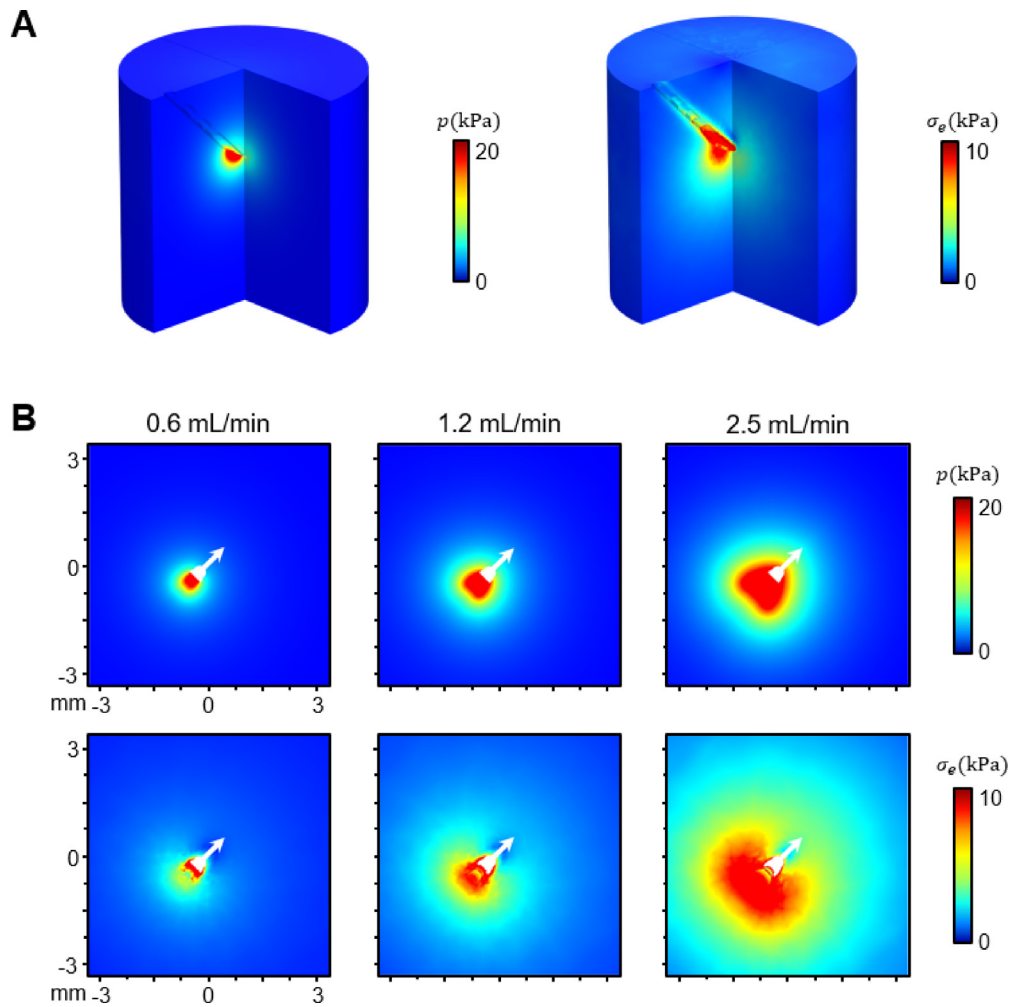
Fig. 6. Computational results of IFP (p) field, and matrix stress (σ_e) field of ETC. (A) 3D distribution of pressure (p) field, and matrix stress (σ_e) field in ETC for 1.2 mL min^{-1} at $t = 0.4$ s. (B) Top view of the pressure and stress fields at the injection flow rates of 0.6, 1.2, and 2.5 mL min^{-1} at $t = 0.4$ s.

response from sensory neurons was found to increase by ∼300% with increasing displacement rate from 560 to 800 μm s^{-1} [41]. In our study, the maximum displacement rates were approximately 400, 600, and 1100 μm s^{-1} at the water injection rates of 0.6, 1.2, and 2.5 mL min^{-1}, respectively, which indicates the 2.5 mL min^{-1} injection may induce the most significant mechanical stimulation with the maximum displacement rate >800 μm s^{-1}.

Stretch-based stimulation is one kind of widely applied mechanical stimuli to study the nociceptive threshold of sensory neurons, and the displacement (stretch) threshold was found to be approximately 14% [42]. In our study, the maximum total displacement significantly increases from approximately 70 to 240 μm (corresponding to approximately 20% to 75%) with increasing injection rate from 0.6 to 2.5 mL min^{-1}. Assuming that the threshold is 14% [42], the above-threshold tissue area significantly increases from approximately 10% to 50% with increasing injection flow rate from 0.6 to 2.5 mL min^{-1}.

The mechanical force and pressure regimes in which neurons respond to mechanical stimuli have been studied recently, and the threshold of the pressure applied to neurons was approximately 6 kPa for transient responses and 9 kPa for sustained responses [43]. It is observed from the computational results that approximately 1% of the collagen area in the vertical cross section crosses this 9 kPa pressure threshold for 0.6 mL min^{-1}. The region above this threshold increases to approximately 3% and 10% for 1.2 mL min^{-1} and 2.5 mL min^{-1} flow rates respectively.

The result confirms that a slower flow rate causes lower magnitudes of the identified IPD biomarkers, which corresponds to the result of patient self-rating that a slower flow rate was associated with lower pain intensity [16]. Moreover, patient's pain experience is usually complex and cannot be reflected by simple pain rating scales. High displacement rate may result in acute but transient pain, while low displacement rate with large tissue swelling area may induce blunt but sustained pain. Thus, the identification and quantification of these different types of biomarkers can be useful to explain patient's complex pain experience and act as a more efficient pain assessment tool.

5. Conclusion

In order to deal with the injection-induced pain which hinders the broader use of biologics and patients' life quality, the development of less-invasive injection devices is necessary but not adequate because the pain caused by injected biologics usually dominates over the sting of needle. Motivated by bridging the knowledge gap between SQ injection and the induced pain, we develop an in-vitro SQ injection model which enables the quantitative measurements of injection-induced mechanical changes in the skin microenvironment, including displacement rate, total displacement, interstitial fluid pressure, and matrix stress. Besides the injection rates and molecular size of biologics studied,
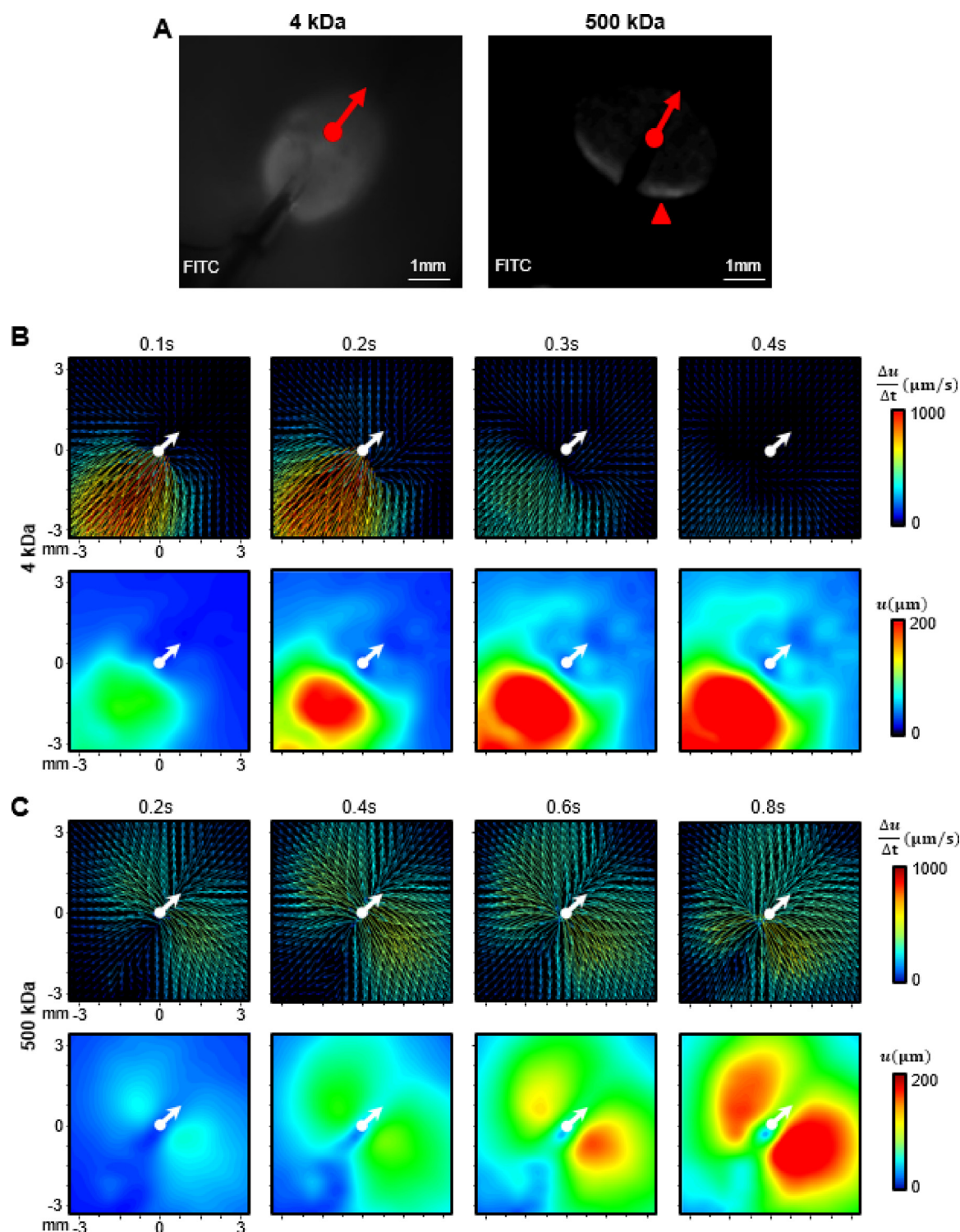
Fig. 7. Effect of molecular weight on the distributions of model biologics and tissue deformation. (A) Spatial distribution patterns of model biologics in ETCs. The injection site is marked by a dot, and the injection direction is indicated by the arrow. The regions where 500 kDa dextran densely accumulated is indicated by a triangle. Displacement rate ($\Delta u/\Delta t$) and total displacement (u) fields induced by the injections of model biologics of (B) 4 kDa and (C) 500 kDa dextran solutions at the injection rate of 1.2 mL min^{-1}.

the developed model is capable of testing other injection parameters including total volume, concentration, molecular weight, and viscosity of drug formulations. The identified potential biomarkers are able to correlate tissue's mechanical microenvironment changes with various SQ injection conditions. Moreover, since patients' pain experience is usually complex and cannot be reflected solely by self-reporting pain rating scales, combined with the commonly used patients' self-rating of pain, the different types of biomarkers can be useful to explain patient's complex pain experience and act as a more efficient pain assessment tool. Finally, the identified biomarkers can be compared with the nociceptive thresholds of sensory neurons evoked by specific kinds of mechanical stimuli, and thus they show promising potential for the further development of the integrated IPD model composed

of both mechanical and nociceptive components, which would be able to identify composite biomarkers to guide the design of drug formulations and injection protocols for minimized pain.

Declaration of competing interest

The authors declare that they have no known competing financial interests or personal relationships that could have appeared to influence the work reported in this paper.

Data availability

Data will be made available on request.

Acknowledgments

Appendix A. Supplementary data

Supplementary material related to this article can be found online at https://doi.org/10.1016/j.eml.2023.102025.

References

[1] B. Shanmugaraj, A. Malla, W. Phoolcharoen, Emergence of novel coronavirus 2019-nCoV: need for rapid vaccine and biologics development, Pathogens 9 (2020) 148.

[2] P. Charoenphol, K. Oswalt, C.J. Bishop, Therapeutics incorporating blood constituents, Acta Biomater. 73 (2018) 64–80.

[3] A.L. Grilo, A. Mantalaris, The increasingly human and profitable monoclonal antibody market, Trends Biotechnol. 37 (2019) 9–16.

[4] Y. Li, D. Stern, L.L. Lock, J. Mills, S.-H. Ou, M. Morrow, X. Xu, S. Ghose, Z.J. Li, H. Cui, Emerging biomaterials for downstream manufacturing of therapeutic proteins, Acta Biomater. 95 (2019) 73–90.

[5] L. Urquhart, Top companies and drugs by sales in 2021, Nat. Rev. Drug Discov. 21 (2022) 251.

[6] E.K. Tetteh, S. Morris, Evaluating the administration costs of biologic drugs: development of a cost algorithm, Health Econ. Rev. 4 (2014) 26.

[7] G.B. Jones, D.S. Collins, M.W. Harrison, N.R. Thyagarajapuram, J.M. Wright, Subcutaneous drug delivery: An evolving enterprise, Sci. Transl. Med. 9 (2017) eaaf9166.

[8] A.C. Anselmo, Y. Gokarn, S. Mitragotri, Non-invasive delivery strategies for biologics, Nat. Rev. Drug Discov. 18 (2019) 19–40.

[9] R. Aronson, The role of comfort and discomfort in insulin therapy, Diabetes Technol. Ther. 14 (2012) 741–747.

[10] T. Heise, L. Nosek, S. Dellweg, E. Zijlstra, K.A. Præstmark, J. Kildegaard, G. Nielsen, T. Sparre, Impact of injection speed and volume on perceived pain during subcutaneous injections into the abdomen and thigh: a single-centre, randomized controlled trial, Diabetes Obes. Metab. 16 (2014) 971–976.

[11] M.-C. Chen, M.-H. Ling, S.J. Kusuma, Poly-γ-glutamic acid microneedles with a supporting structure design as a potential tool for transdermal delivery of insulin, Acta Biomater. 24 (2015) 106–116.

[12] J.R. Curtis, C. Hobar, K. Hansbrough, Injection-site burning and stinging in patients with rheumatoid arthritis using injectable biologics, Curr. Med. Res. Opin. 27 (2011) 71–78.

[13] T. Matsui, R. Umetsu, Y. Kato, Y. Hane, S. Sasaoka, Y. Motooka, H. Hatahira, J. Abe, A. Fukuda, M. Naganuma, Age-related trends in injection site reaction incidence induced by the tumor necrosis factor-α (TNF-α) inhibitors etanercept and adalimumab: the Food and Drug Administration adverse event reporting system, 2004–2015, Int. J. Med. Sci. 14 (2017) 102.

[14] T. Yoshida, Y. Otaki, N. Katsuyama, M. Seki, J. Kubota, New adalimumab formulation associated with less injection site pain and improved motivation for treatment, Mod. Rheumatol. 29 (2019) 949–953.

[15] P. Nash, J. Vanhoof, S. Hall, U. Arulmani, R. Tarzynski-Potempa, K. Unnebrink, A.N. Payne, A. Cividino, Randomized crossover comparison of injection site pain with 40 mg/0.4 or 0.8 mL formulations of adalimumab in patients with rheumatoid arthritis, Rheumatol. Ther. 3 (2016) 257–270.

[16] M. Jain, D. Doughty, C. Clawson, X. Li, N. White, B. Agoram, R. van der Merwe, Tralokinumab pharmacokinetics and tolerability when administered by different subcutaneous injection methods and rates, Int. J. Clin. Pharmacol. Ther. 55 (2017) 606.

[17] P. Delmas, J. Hao, L. Rodat-Despoix, Molecular mechanisms of mechanotransduction in mammalian sensory neurons, Nat. Rev. Neurosci. 12 (2011) 139–153.

[18] K.Y. Teo, J.C. Dutton, B. Han, Spatiotemporal measurement of freezing-induced deformation of engineered tissues, J. Biomech. Eng. 132 (2010) 031003.

[19] B. Han, J.D. Miller, J.K. Jung, Freezing-induced fluid-matrix interaction in poroelastic material, J. Biomech. Eng. 131 (2009) 021002.

[20] K.Y. Teo, T.O. DeHoyos, J.C. Dutton, F. Grinnell, B. Han, Effects of freezing-induced cell–fluid–matrix interactions on the cells and extracellular matrix of engineered tissues, Biomaterials 32 (2011) 5380–5390.

[21] A. Ozcelikkale, K. Shin, V. Noe-Kim, B.D. Elzey, Z. Dong, J.-T. Zhang, K. Kim, I.C. Kwon, K. Park, B. Han, Differential response to doxorubicin in breast cancer subtypes simulated by a microfluidic tumor model, J. Control. Release 266 (2017) 129–139.

[22] M. Geerligs, L. Van Breemen, G. Peters, P. Ackermans, F. Baaijens, C. Oomens, In vitro indentation to determine the mechanical properties of epidermis, J. Biomech. 44 (2011) 1176–1181.

[23] I.D. Johnston, D.K. McCluskey, C.K.L. Tan, M.C. Tracey, Mechanical characterization of bulk Sylgard 184 for microfluidics and microengineering, J. Micromech. Microeng. 24 (2014) 035017.

[24] C. Li, G. Guan, R. Reif, Z. Huang, R.K. Wang, Determining elastic properties of skin by measuring surface waves from an impulse mechanical stimulus using phase-sensitive optical coherence tomography, J. R. Soc. Interface 9 (2012) 831–841.

[25] B.A. Roeder, K. Kokini, J.E. Sturgis, J.P. Robinson, S.L. Voytik-Harbin, Tensile mechanical properties of three-dimensional type I collagen extracellular matrices with varied microstructure, J. Biomech. Eng. 124 (2002) 214–222.

[26] M.D.C. Lopez-Garcia, D.J. Beebe, W.C. Crone, Young's modulus of collagen at slow displacement rates, Bio-Med. Mater. Eng. 20 (2010) 361–369.

[27] V. Normand, D.L. Lootens, E. Amici, K.P. Plucknett, P. Aymard, New insight into agarose gel mechanical properties, Biomacromolecules 1 (2000) 730–738.

[28] D. Farrar, D.J. Tuffnell, J. West, H.M. West, Continuous subcutaneous insulin infusion versus multiple daily injections of insulin for pregnant women with diabetes, Cochrane Database Syst. Rev. (6) (2016).

[29] B.M. Torrisi, V. Zarnitsyn, M.R. Prausnitz, A. Anstey, C. Gateley, J.C. Birchall, S.A. Coulman, Pocketed microneedles for rapid delivery of a liquid-state botulinum toxin a formulation into human skin, J. Control. Release 165 (2) (2013) 146–152.

[30] C.E. Henry, Y.-Y. Wang, Q. Yang, T. Hoang, S. Chattopadhyay, T. Hoen, L.M. Ensign, K.L. Nunn, H. Schroeder, J. McCallen, Anti-PEG antibodies alter the mobility and biodistribution of densely pegylated nanoparticles in mucus, Acta Biomater. 43 (2016) 61–70.

[31] G. Casi, D. Neri, Antibody–drug conjugates: Basic concepts, examples and future perspectives, J. Control. Release 161 (2) (2012) 422–428.

[32] L. Sanavia, B.A. Schrefler, P. Steinmann, Geometrical and material nonlinear analysis of fully and partially saturated porous media, in: Porous Media, Springer, 2002, pp. 341–381.

[33] Y. Leng, M. de Lucio, H. Gomez, Using poro-elasticity to model the large deformation of tissue during subcutaneous injection, Comput. Methods Appl. Mech. Engrg. 384 (2021) 113919.

[34] S. Bose, S. Li, E. Mele, V.V. Silberschmidt, Dry vs. wet: Properties and performance of collagen films. Part I. Mechanical behaviour and strain-rate effect, J. Mech. Behav. Biomed. Mater. 111 (2020) 103983.

[35] F.J. O'Brien, B.A. Harley, M.A. Waller, I.V. Yannas, L.J. Gibson, P.J. Prendergast, The effect of pore size on permeability and cell attachment in collagen scaffolds for tissue engineering, Technol. Health Care 15 (2007) 3–17.

[36] S. Ramanujan, A. Pluen, T.D. McKee, E.B. Brown, Y. Boucher, R.K. Jain, Diffusion and convection in collagen gels: implications for transport in the tumor interstitium, Biophys. J. 83 (2002) 1650–1660.

[37] L. Mohee, G.S. Offeddu, A. Husmann, M.L. Oyen, R.E. Cameron, Investigation of the intrinsic permeability of ice-templated collagen scaffolds as a function of their structural and mechanical properties, Acta Biomater. 83 (2019) 189–198.

[38] T. Fischer, A. Hayn, C.T. Mierke, Fast and reliable advanced two-step pore-size analysis of biomimetic 3D extracellular matrix scaffolds, Sci. Rep. 9 (2019) 1–10.

[39] S.J. Lee, G.L. Pishko, G.W. Astary, T.H. Mareci, M. Sarntinoranont, Characterization of an anisotropic hydrogel tissue substrate for infusion testing, J. Appl. Polym. Sci. 114 (2009) 1992–2002.

[40] A. Pluen, P.A. Netti, R.K. Jain, D.A. Berk, Diffusion of macromolecules in agarose gels: comparison of linear and globular configurations, Biophys. J. 77 (1999) 542–552.

[41] J. Hao, P. Delmas, Multiple desensitization mechanisms of mechanotransducer channels shape firing of mechanosensory neurons, J. Neurosci. 30 (2010) 13384–13395.

[42] M.R.C. Bhattacharya, D.M. Bautista, K. Wu, H. Haeberle, E.A. Lumpkin, D. Julius, Radial stretch reveals distinct populations of mechanosensitive mammalian somatosensory neurons, Proc. Natl. Acad. Sci. USA 105 (2008) 20015–20020.

[43] B.M. Gaub, K.C. Kasuba, E. Mace, T. Strittmatter, P.R. Laskowski, S.A. Geissler, A. Hierlemann, M. Fussenegger, B. Roska, D.J. Müller, Neurons differentiate magnitude and location of mechanical stimuli, Proc. Natl. Acad. Sci. USA 117 (2020) 848–856.